



# WAVE-E

## WATER Vapour European-Explorer

N. Arago-Higueras, O. Bylund, M. Deiml, D. Jimenez-Lluva, J. Jobling, A. Karnthaler, T. F. Klingenberg, M. Link, P. Niemelä, D. Paraiso, C. Pauna, S. Pavesi, S. Rourke, S. Scheiblaue, M. Aguirre and A. Al Bitar

Date: July 20, 2016

### ABSTRACT

The stratosphere, and in particular the dynamics within it, has a huge impact on surface parameters that directly affect water and the water cycle, and therefore can cause extreme weather events. Dynamics of the Upper Troposphere Lower Stratosphere (UTLS) region have an enormous impact on the polar jet stream and therefore on the North Atlantic Oscillation (Kidston *et al.* 2015). UTLS effects at the surface are more accurately predicted when initialized daily with well resolved stratospheric observations (Marshall and Scaife 2010). However, due to the combination of the high stratification of the UTLS region and the low vertical resolution of observations, operational numerical weather prediction and climate models are currently poorly constrained by observations in this region (Müller *et al.* 2016). A better understanding of UTLS coupling will enhance our knowledge of atmospheric processes that affect the water cycle and improve weather forecasts and climate models. This helps to prevent damage, and reduce costs through safety precautions before extreme weather events (Jiang *et al.* 2015).

In this report, the authors propose the WATER Vapour European - Explorer (WAVE-E) satellite mission to monitor water vapour in the UTLS to help answer the water cycle related science questions presented above. The WAVE-E mission consists of three small (~ 480kg) satellites that will be put on sun-synchronous LEO orbits. The main instrument onboard WAVE-E(1,2,3) is a limb sounding and cross-track scanning mid-infrared passive spectrometer (824 $cm^{-1}$  to 829 $cm^{-1}$ ). The WAVE-E mission will provide water vapour products over the UTLS region at a 1 km vertical resolution and 25 km horizontal resolution. Synergistic use of WAVE-E and MetOp-NG operational satellites is identified, knowing that neither mission is dependent on the other and that WAVE-E does not impose any requirements on MetOp. The combination of data from WAVE-E and IASI-NG onboard MetOp-NG in a data fusion retrieval algorithm is expected to provide water vapour profiles from the surface to the lower stratosphere.

**Key words.** water vapour – UTLS – water cycle – limb sounding – DASH – spectrometry

## 1. Introduction

Driven mostly by solar heating, water evaporates from ocean and land surfaces, is carried by the winds, and condenses to form clouds and precipitation that falls to land and oceans. The precipitation that falls over land may be stored temporarily either as snow or soil moisture, while the remaining precipitation (in the form of rainfall), runs off to form streams and rivers. These discharge the freshwater into the oceans, thereby completing the global water cycle (Trenberth *et al.* 2007). The changing water cycle is among the most serious issues confronting scientists and society today. It is therefore necessary to improve the observation of critical water cycle elements in order to close gaps in process understanding and to advance the representation of the water cycle in Earth system models. The atmosphere is an essential part of Earth's water cycle. Water vapour, the result of evaporation and transpiration, plays a crucial role in Earth's climate, and it is the most significant greenhouse gas in the Earth's atmosphere, accounting for about 50 % of the greenhouse gases (Held and Soden 2000; Schmidt *et al.* 2010; Müller *et al.* 2016).

Tropical thunderstorms cause a mixing of air between the Upper Troposphere and Lower Stratosphere (UTLS), driving a mass transport of air from lower to higher latitudes, causing variability of water vapour in this region. However, the dynamics in this region of the atmosphere are poorly understood, despite it being the most relevant region for the radiative forcing of surface climate (Kidston *et al.* 2015; Müller *et al.* 2016). The

stratosphere, and especially the stratospheric dynamics, has huge impacts on surface parameters that directly affect water and the water cycle and therefore can cause extreme weather events. A better understanding of the stratosphere and its coupling to the troposphere will not only enhance our knowledge of atmospheric processes that affect the water cycle, but also will improve the capability for better weather forecasts and climate models to prevent damage, and reduce costs through safety precautions before extreme weather events (Jiang *et al.* 2015).

Due to the combination of the high stratification of the UTLS region and the low vertical resolution of observations, operational numerical weather prediction and climate models are currently poorly constrained by observations in this region (Gerber *et al.* 2009). In the following report, we propose a satellite mission to monitor water vapour in the UTLS region in order to gather crucial data in high resolution to improve our knowledge of atmospheric dynamics which impact the Earth's water cycle.

It has been outlined in ESA's "Earth Observation and Water Cycle Science Priorities" document from October 2015, that the observation of water vapour in the UTLS region should be prioritised. The challenge is to measure water vapour over a climatological time period in a consistent and homogeneous manner to improve the quality of currently available climate data records, and to better constrain energy and water cycle closure studies. In response to this challenge, it was suggested that a combination of multi-satellite, multi-sensor, and multi-agency observation and reanalysis data should be used. In particular, it was emphasised

that there was a need to focus on the UTLS region, both because of its climate sensitivity and because the Coupled Model Intercomparison Project (CMIP) and reanalysis models are too wet compared to observations in this region (e.g. from MLS) (ESA-GWEX 2015). Although there is a need for water vapour observations over a climatological time period, the authors first propose an Earth explorer mission for water vapour in the UTLS region which may pave the way for a future operational mission.

## 2. Science

### 2.1. Earth's atmosphere and its dynamics

The dynamical links between the stratosphere and troposphere exert a significant downward influence and affect the surface weather. However, this region is poorly quantified and poorly understood for three main reasons. Firstly, there is sparse and discontinuous coverage of global UTLS water vapour observations, leading to a low confidence in global long-term trends (Hegglin *et al.* 2014). Secondly, the tropopause fluctuates in altitude, making trends at constant altitudes difficult. Finally, deep convective transport from the tropics moisten the lower stratosphere at mid-latitudes, causing variability of water vapour in this region. This lack of understanding is a particular problem, as it has been shown that the UTLS region is most relevant for surface climate (Müller *et al.* 2016).

Strong uplift in the intertropical convergence zone excite the stable UTLS region, causing low frequency gravity waves. These waves transfer momentum towards the poles and modify the strength the polar stratospheric jet. Intensified jet streams can result in extreme rainfall, flooding, and low temperatures at mid-latitudes (Tripathi *et al.* 2016). On the other hand, weakened jet streams and increased north-south meandering of the jet stream can give rise to slow moving weather systems, causing heat waves and droughts (Hassanzadeh *et al.* 2014).

The authors propose to investigate water vapour trends and use it as an indicator for UTLS dynamics which influence the water cycle (e.g., low frequency gravity waves) because it is an Essential Climate Variable (ECV), a greenhouse gas and a passive gas (Hartmann *et al.* 2013).

### 2.2. Science Objectives and Measurement Requirements

As stated above, a better understanding of the UTLS dynamics will yield to better Earth system model skills, and thus a better understanding of extreme weather events. More comprehensive data will provide an important contribution for weather forecasts and mitigation of the impact hydrological hazards. Satellite data (Fig. 1 a) has lower uncertainty compared to monthly balloon-sounding (Fig. 1 b, green dots) and provides global coverage. To understand global trends in water vapour and UTLS dynamics, it is essential to establish continuous satellite measurements.

The scientific objectives of the WAVE-E mission are to monitor water vapour profiles in the UTLS at high vertical and temporal resolution to:

- Improve knowledge on short-term and seasonal weather phenomena and help mitigate the effects of hydrological hazards linked to the UTLS (e.g., floods, droughts)
- Improve knowledge on mid-term and seasonal weather phenomena and help mitigate the effects of hydrological hazards (e.g., Monsoon, ENSO)
- Obtain a long-term data set to understand the impact of UTLS water vapour on the radiative budget of the Earth

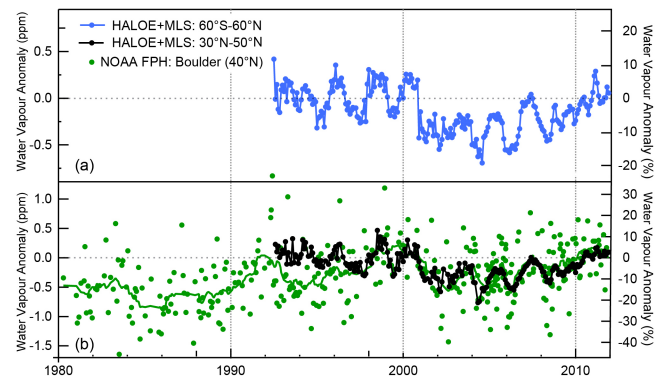


**Fig. 1.** Water vapour anomalies in the lower stratosphere ( $\sim 16$  to  $19$  km) from satellite sensors and in situ measurements normalized to 2000–2011. (a) Monthly mean water vapour anomalies at 83 hPa for  $60^{\circ}\text{S}$  to  $60^{\circ}\text{N}$  (blue) determined from HALOE and MLS satellite sensors. (b) Approximately monthly balloon-borne measurements of stratospheric water vapour from Boulder, Colorado at  $40^{\circ}\text{N}$  (green dots; green curve is 15-point running mean) averaged over 16 to 18 km and monthly means as in (a), but averaged over  $30^{\circ}\text{N}$  to  $50^{\circ}\text{N}$  (black). Figure and caption from Hartmann *et al.* (2013).

- Develop a coherent theory of stratosphere-troposphere coupling

An overview of the science requirements and the justification is summarised in Table 1. Constraining the models frequently with highly vertically resolved UTLS measurements will improve the numerical weather prediction of short term events.

The need for higher vertical resolution of water vapour in the UTLS region is a priority for the global cycle, and should be less than 2 km (Müller *et al.* 2016). However, ESA-GWEX (2015) outlined a need for 1 km resolution, based on the high stratification of the UTLS region.

Temporal resolution is important because the dynamic variations in the speed of the stratospheric jet almost instantaneously affects the troposphere Kidston *et al.* (2015), and therefore changing precipitation regimes and evapotranspiration patterns. Enhancing models with homogeneously distributed global UTLS water vapour observations will aid in understanding and investigating, for example, the global stratospheric teleconnection pathway between the Pacific and Europe. The temporal resolution required to detect upper tropospheric water vapour trends is increased by measurement frequency, more than measurement accuracy (Müller *et al.* 2016). The residence time of water in the atmosphere is approximately 10 days (Bolin and Rodhe 1973). However, atmospheric dynamics occur on much shorter time scales. For example, tropical thunderstorms, which drive large-scale circulation, occur on scales in the order of hours. For this water cycle mission, a temporal resolution in the range of 3-6 hours is chosen. With this temporal resolution, the observations can be used to enhance ECMWF's High Resolution or Ensemble models (Andersson 2015), for example. This will help to improve current knowledge about UTLS dynamics, which drive extreme precipitation events. Marshall and Scaife (2010) outlined that daily initialization of models with stratospheric observations is beneficial for seasonal forecasting of surface events due to Sudden Stratospheric Warming events. It should be noted that the exact temporal resolution required to observe water vapour trends is not known. Müller *et al.* (2016) outlined the need for theoretical studies based on hypothetical water vapour time series to better estimate this requirement.

**Table 1.** Traceability Matrix

Objectives	Measurement Requirements	References
<b>PSO.1:</b> Monitor water vapour profiles in the UTLS at high vertical resolution to improve knowledge on short-term weather events	<b>SR1.1:</b> < 2 km vertical resolution <b>SR1.2:</b> 9-36 km horizontal resolution <b>SR1.3:</b> < 6 h temporal resolution <b>SR1.4:</b> Uncertainty <10%	Müller <i>et al.</i> (2016) ECMWF HRES/ENS Müller <i>et al.</i> (2016) Waterfall A. (2012)
<b>PSO.2:</b> Monitor water vapour profiles in the UTLS at high vertical resolution to improve knowledge on seasonal weather events	<b>SR2.1:</b> < 2 km vertical resolution <b>SR2.2:</b> 18-36 km horizontal resolution <b>SR2.3:</b> 12 h temporal resolution	Müller <i>et al.</i> (2016) ECMWF ENS Marshall and Scaife (2010)
<b>SSO1:</b> Obtain a long-term dataset of vertically resolved UTLS water vapour to understand the impact of UTLS water vapour on Earth’s radiative budget	<b>SG2.1:</b> 11 years mission duration (duration of Solar Cycle)	IPCC report
<b>SSO2:</b> Development of a coherent theory of stratosphere-troposphere coupling	<b>SG2.2:</b> long term mission duration	Kidston <i>et al.</i> (2015)

**3. Payload**

The payload of the Water Vapour European - Explorer (WAVE-E) is based on a limb viewing and cross-track scanning Infra-Red (IR) spectrometer. This payload allows the scientific requirements (as described above) to be fulfilled. In the following sections, the observation strategy, the measurement principle, a preliminary Signal-to-Noise (S/N)-ratio analysis and the instrument with its most important subsystems are described.

**3.1. Observation Strategy**

Three satellites are proposed to fly in a constellation to achieve a high temporal resolution and to provide limb measurements. Thereby, the baseline observation strategy does not rely on any other satellite. However, the orbit parameters are chosen that the tangent points are directly below the MetOP satellite, respectively below the American operational meteorology satellites (EUMETSAT 2016) in Sun-synchronous Low Earth Orbit (LEO). Thus, synergies can be utilized without imposing any requirements on these operational satellites.

Each instrument is observing a tangential altitude between 5km and 25km in a limb viewing geometry with a resolution of 1km. The observation geometry is shown in Figure 2. This observation strategy allows synergies with the Infrared Atmospheric Sounding Interferometer (IASI) instrument onboard MetOP (Clerbaux *et al.* 2009), and the IASI-NG instrument on MetOP-NG (Crevoisier *et al.* 2014). The IASI instruments provide precise water vapor information in the lower troposphere with a resolution of approximately 1km (Herbin *et al.* 2009). The instrument onboard WAVE-E extends this range up from 5km to 25km. WAVE-E will fly in front of MetOP to reduce straylight from the sun, and to protect the optics from atomic oxygen.

The instrument provides cross-track scanning with a swath-width of 2130km, similar to IASI (OSCAR 2016), to provide 4h for a constellation of three satellites. Figure 3 shows a top view of the observation strategy. The cross-track resolution of the instrument is 25km; by tilting the beam by approximately 18°, the required swath-width is achieved. The aim of an along-track horizontal resolution of 50km using fast sampling and tomographic retrieval routines is envisioned, similar to the PREMIER mission (ESA 2012). A vertical resolution of 1km within the 20km observation range is achieved within the spectrometer, as it is further detailed in chapter 3.4.2.

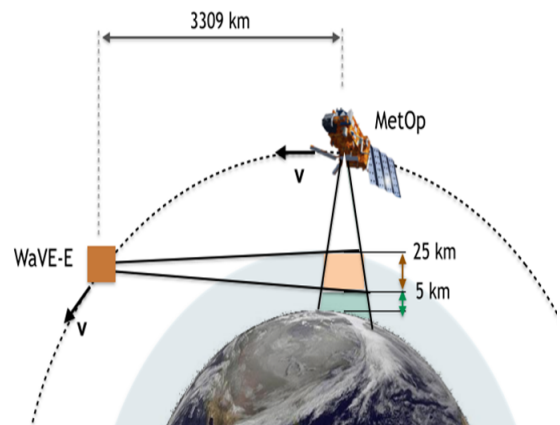


**Fig. 2.** Side view of the observation strategy for WAVE-E. The blue area is measured by the IASI instrument of MetOP and the orange area is measured by WAVE-E.

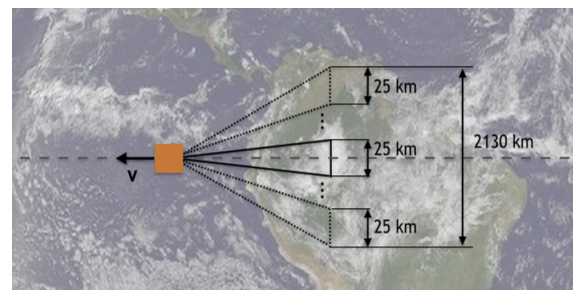


**Fig. 3.** Top view of the observation strategy for WAVE-E.

**3.2. Measurement Principle**

Radiance in the mid-IR between  $824cm^{-1}$  and  $829cm^{-1}$  (approximately  $12\mu m$ ) is measured with a spectral resolution of  $0.08cm^{-1}$ . Figure 4 shows the spectral radiance of two water vapour emission lines at an apparent tangent height of 10km (9.37km refracted tangent height) in the spectral range (green line), as well as the combined emission of the important species  $O_3$ ,  $CO_2$ ,  $N_2O$ ,  $O_2$  and  $CH_4$  (shown by the blue line). These two lines have also been used by MIPAS for water vapour retrieval (von Clarmann *et al.* 2009). The upper and lower detection limits of the instrument are shown with dashed lines. The simulation uses the US standard atmosphere (NOAA 1976) and the Hitran 2012 spectroscopy database (Rothman *et al.* 2013), and is performed with the tool Spectral Calc.

The integrated spectral radiance of water vapour emission was used in a Monte-Carlo simulation with 1000 samples to cal-

calculate the dependence between S/N-ratio for a water vapour content of  $70\text{ppm}$  at an altitude of  $10\text{km}$ . The noise is assumed to be 50% multiplicative and 50% additive. Water vapour is the only retrieval variable; considering the selected bandwidth, the intensity between water vapour content and spectral radiance is assumed to be linear. This analysis provides a first estimate on the required S/N-ratio from the instrument perspective. As shown in Figure 5, the standard deviation of the water vapour retrieval uncertainty lies at approximately  $100\text{ppm}$  for an S/N-ratio of 60. The science requirement of an uncertainty lower than 10% is achieved with a measurement uncertainty lower than  $2300\text{ppm}$  ( $3\sigma$ ). Thus, achieving a S/N-ratio better than 60 with the resulting measurement uncertainty of  $100\text{ppm}$  shows that the scientific requirement will be fulfilled, with a high factor of safety for an altitude up to  $10\text{km}$ . Future studies propagating the errors from end-to-end while taking in consideration the scene dependent state variables in the atmosphere will be needed, to have a full estimate of the error budget.

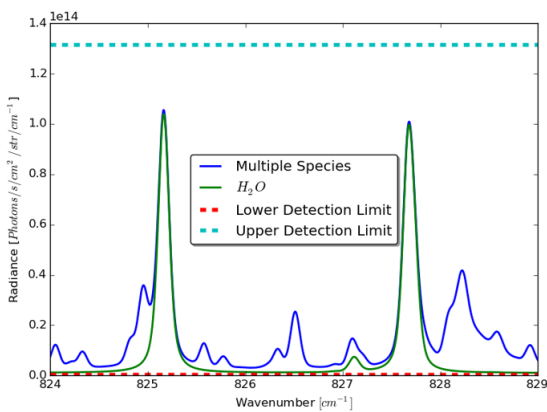


**Fig. 4.** Radiance in dependence of wavenumber for  $H_2O$  (green line) and  $H_2O$  including the species  $O_3$ ,  $CO_2$ ,  $N_2O$ ,  $O_2$  and  $CH_4$  (blue line) in addition to upper and lower detection limit (dashed lines)

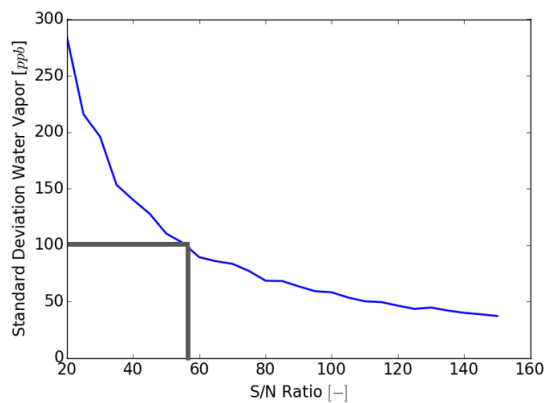


**Fig. 5.** Water vapour measurement uncertainty ( $1\sigma$ ) in dependence of S/N-ratio calculated by a Monte-Carlo simulation with 1000 samples.

### 3.3. S/N-Ratio Analysis

Using information on water vapour radiance and the required S/N-ratio from Chapter 3.2, the instrument is analysed to show that this requirements can be fulfilled. Table 2 provides an overview of the received radiance, which is converted to radi-

ant flux, including a factor of safety of 10 and an étendue of  $1.62 \times 10^{-3}$  per pixel row. Hence a pixel row corresponds to a spectrum for a specific altitude. The étendue is calculated with a Field of View (FOV) corresponding to the observation strategy (Chapter 3.1) and an entrance aperture area of  $15\text{cm}$ . The radiant flux is further converted into a signal by multiplication with a detector quantum efficiency of  $0.8e^-/\text{photons}$ , and a transmissivity of the whole system of 40%. The interferogram consists of 400 pixels and the integration time is  $0.3\text{s}$ ; from these values, the integrated signal can be calculated. As shown in Figure 4, the spectrum does not only consist of radiance from  $H_2O$ , but also from other sources. In the peaks of the  $H_2O$  emission, this radiance equals  $1.17\%$  or  $60e^-$  as stated in the table. The calibration error with 1% is assumed to be similar to the MIPAS experiment (Endemann 1999). The readout noise and the dark current specify detector requirements that finally lead to a S/N-ratio of approximately 70 in addition to the shot noise, and thus is deemed sufficient.

**Table 2.** S/N-Ratio Analysis

Name	Value	Unit
Radiance	$1.22 \times 10^{-6}$	$W/cm^2/str$
Factor of Safety	10	-
Radiant Flux	$1.31 \times 10^{10}$	$photons/s$
Total Signal	$6.83 \times 10^6$	$e^-/s$
Signal per Pixel row	$1.71 \times 10^4$	$e^-/s$
Integrated Signal	$5.12 \times 10^3$	$e^-$
Other emission lines	60	$e^-$
Calibration Error	51	$e^-$
Readout Noise	100	$e^-rms$
Dark Current	0.4	$e^-/s$
Shot Noise	72	$e^-rms$
S/N	70	-

### 3.4. Instrument

The analysis and the requirements above allow the selection of suitable sub-components for the instrument. The heart of the instrument is the spectrometer. A Spatial Heterodyne Spectrometer (SHS) has been selected as it can measure a small spectral range with a high spectral resolution, while providing a large FOV and a rigid monolithic design. These advantages make this spectrometer reliable and superior to other spectrometers for this application.

Figure 6 shows a schematic of the complete instrument. Light is entering from the left side and gets reflected by a tilt mirror into a telescope. The mirror can be rotated to achieve the  $\pm 18^\circ$  of cross-track scanning. In addition, it is used for calibration by pointing it into a warm black body, or alternatively to cold space. A telescope reduces the aperture, increases the internal FOV and provides a field stop for stray-light reduction. With two lenses, the beam from the telescope first gets collimated and later focused into the spectrometer. The focusing of the beam is required to achieve the vertical resolution. Afterwards, the spectrometer is imaged onto the detector, where it passes another field stop into the cold box. The detector is connected to the readout electronics and via a cold finger to the cooler. By considering all components of the instrument, the mass, power, volume and data rate budgets for the instrument can be derived, as shown in Table 3. The mass and power values include a maturity factor of 35%.

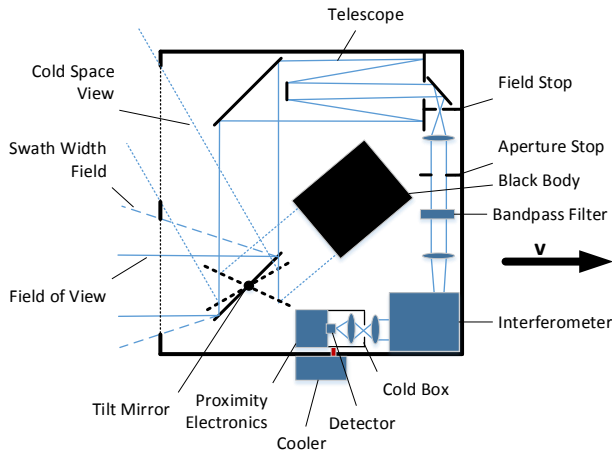


Fig. 6. Schematics of the WAVE-E instrument

Table 3. Instrument properties

Name	Value	Unit
Mass	79	kg
Power	92	W
Volume	$0.8 \times 0.8 \times 0.3$	$m^3$
Data Rate	940	kbit/s

### 3.4.1. Telescope

A Ritchey–Chrétien telescope is employed on the instrument, a specialised variant of the Cassegrain telescope with two hyperbolic mirrors. It has an input aperture of 150mm and an output aperture of 40mm. An alternative was use of a Gregorian telescope, because of its inherent field stop useful for stray light reduction. However, due to the compact design that allows the system to be free of the aberration known as coma, the Ritchey–Chrétien has been chosen as baseline.

### 3.4.2. Spectrometer

Different types of spectrometer have been considered for this instrument. Remote sensing satellites typically use filters and gratings to receive spectral information. Fabry-Perot Spectrometer (FPS) and Michelson Interferometer (MI) are more complex instrument types, which can provide higher light sensitivity - they have a higher étendue, or throughput. The TIMED Doppler Imager (TIDI) (Killeen *et al.* 1999) on the Thermosphere Ionosphere Mesosphere Energetics and Dynamics (TIMED) satellite is stated exemplary for a FPS. Michelson Interferometer for Passive Atmospheric Sounding (MIPAS) (Fischer *et al.* 2008) on-board ENVISAT and WIND Imaging Interferometer (WINDII) (Shepherd *et al.* 1993) for wind measurements have been successfully flown in space as Fourier Transform Spectrometer (FTS).

Another type of FTS has been conceptualised by Connes (1958). However, as a result of improved detector technology, the SHS was re-invented by Harlander *et al.* (1992). Since then, this spectrometer type has been successfully demonstrated in space during a Space Shuttle mission (Harlander *et al.* 2002). Afterwards, it was shown that such a spectrometer can be built as a monolithic block, see Harlander *et al.* (2002) and Doe and Watchorn (2011). The monolithic design is of particular interest, as it reduces the size and mass of the instrument considerably and makes it rigid and less sensitive to vibrations. The instru-

ment MIGHTI onboard the ICON mission, scheduled to launch in 2017, uses a variant of an SHS (Englert *et al.* 2015). Field-widening of the SHS offers another advantage, similar to a MI. This technique increases the étendue of the instrument considerably, allowing the observation of low emitting sources or to reduce the instrument size.

The SHS can be described as a combination of a grating spectrometer and a FTS. It visually appears to be similar to the MI, but the mirrors in the arms are replaced by tilted gratings. Figure 7 illustrates the basic concept of the SHS. Light enters the system from the left and gets divided by a beam splitter. Each beam is diffracted and reflected by a grating (Grating 1, Grating 2).

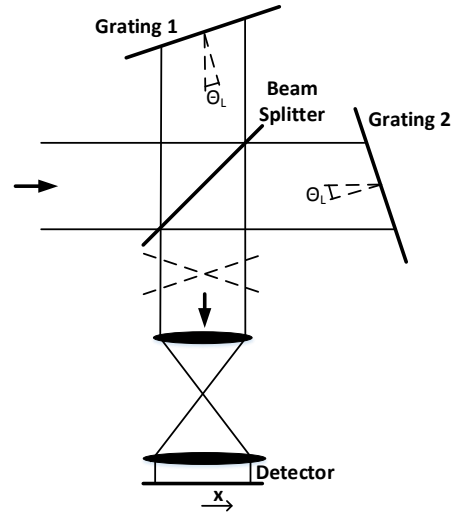


Fig. 7. Schematic of a Spatial Heterodyne Spectrometer (SHS) with beamsplitter, gratings, imaging optics and detector. The two tilted dashed lines represent the wavefronts from the two arms with a wavenumber different than the Littrow wavenumber.

Both gratings are tilted by the Littrow angle  $\theta_L$ . The incoming light is refracted according to equation 1,

$$\sigma (\sin(\theta_L) + \sin(\theta_L - \gamma)) = m/d \quad (1)$$

where  $\sigma$  is the wavenumber of the incoming light in  $cm^{-1}$ ,  $\theta_L$  the Littrow angle,  $\gamma$  the angle of deviation from the Littrow angle for the exiting beam,  $m$  the diffraction order and  $1/d$  the grating groove density. As illustrated in Figure 7, the Littrow angle is chosen such that the reflected radiation exits parallel to the incoming radiation for a specific wavenumber, the Littrow wavenumber  $\sigma_L$ . This Littrow condition is expressed by equation 2.

$$\sin \theta_L = \frac{m}{2d\sigma_L} \quad (2)$$

The two beams are recombined at the beam splitter and uniform interference can be detected at the Focal Plane Array (FPA) for the Littrow wavenumber. For other wavenumbers, the refracted and reflected wavefronts from the two arms are slightly tilted with respect to the incoming wavefront. This results in interference patterns after recombination, caused by the phase differences between the two beams. Figure 7 shows the wavefronts of these two beams after recombination in dashed lines.

The phase difference is zero in the centre of the detector and increases with the distance  $x$ . At a specific distance from the centre, the phase difference becomes  $\pi/2$ , which results in destructive interference. With further increasing distance, maximum constructive interference is observed. Overall, a striped interference pattern (in the  $x$ -direction) is registered by the FPA (Detector in Figure 7). The interferogram is described by equation 3, which represents an inverse Fourier-Transformation of the incoming radiance spectrum  $L(\sigma)$ . The number of intensity maxima and minima for a spectral line depends on the difference of the spectral line's wavenumber  $\sigma$  to the Littrow wavenumber  $\sigma_L$ . This describes the 'heterodyning' aspect of the SHS. The spatial frequency on the detector is expressed by equation 4 for a specific spectral line with wavenumber  $\sigma$ .

$$I_g(x) = \int_0^{\infty} 0.5L(\sigma)(1 + \cos(8\pi \tan \theta_L x(\sigma - \sigma_L)))d\sigma \quad (3)$$

$$\nu_F = 4 \tan \theta_L(\sigma - \sigma_L) \quad (4)$$

Imaging a scene with an anamorphic telescope, the detector dimension, orthogonal to the spectral direction, can be used as spatial dimension, as demonstrated by Englert *et al.* (2005). The SHS can therefore be used to detect the vertical intensity distribution of the  $H_2O$  emission in limb viewing geometry. Field-widening of a SHS is simpler, compared to the complex field-widening mechanism required for a MI; see Shepherd (2002). Two stationary prisms between the gratings and the beam splitter allow for increasing the FOV in the order of two magnitudes by virtually rotating the image of the gratings perpendicular to the optical axis. A monolithic design of a field-widened SHS is shown in Figure 8. One arm consists of a spacer between beam splitter and prism (spacer 1), the field widening prism and a second spacer (spacer 2) between prism and grating. The spacers are hollow parts, so that they do not interfere with the light beam. These three arm elements have slanted angles as shown in Figure 8, which also shows also the optical axis with dash-dotted lines. Table 4 summarises the key properties of the SHS.

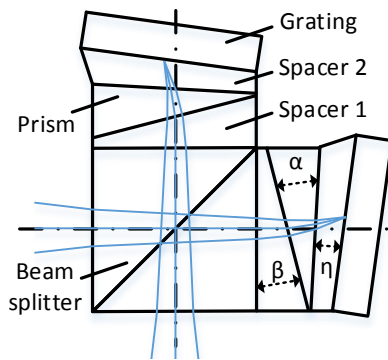


**Fig. 8.** Schematic of a field-widened Spatial Heterodyne Spectrometer (SHS) with beam splitter, spacer 1, field-widening prism, spacer 2 and gratings (Top View).

### 3.4.3. Detector

A Mercury Cadmium Telluride (MCT) detector was selected for data spectrometer acquisition due to its good detection performance in the long infrared wavelength region (approximately  $1.1 \times 10^{10} \text{ cmHz}^{-1/2} \text{ W}^{-1}$  around  $12\mu\text{m}$ ). MCT detectors have also

**Table 4.** Attributes of the spectrometer

Attribute	Design
Littrow Wavenumber $\sigma_L$	$810 \text{ cm}^{-1}$
Grating Groove Density $1/d$	$150 \text{ lines/mm}$
Diffraction Order $m$	1
Aperture height $d$	$40 \text{ mm}$

high quantum efficiency ( $> 80\%$ ), low readout noise ( $< 100e^-$ ) and dark current ( $< 0.4e^-/s$ ) compared to other detector types, and a high Technology Readiness Level (TRL) with flight heritage, as evident in (Nibir K. Dhar 2013). The detector and cold box need to be cooled down to approximately  $80\text{K}$  to achieve the required S/N-ratio during operations. For this purpose, an active Stirling-based cryocooler was selected. This cryocooler is capable of cooling the detector itself, as well as the cold box around it which is to prevent stray-light from hitting the detector. Total required cooling power is estimated to be  $850\text{mW}$ . Further analysis showed that passive cooling is a viable alternative, if the vibrations caused by the compressor in the Stirling cooler ultimately affect the instrument's performance. The resulting increase in total volume and mass of the cooling system would be acceptable.

### 3.4.4. Calibration

The calibration concept of the instrument is based on linear interpolation between a hot and cold source, as employed routinely by satellites, for example (Endemann 1999). The cold source is space with a temperature of approximately  $3\text{K}$  and the warm source is provided by an internal black body with a temperature around  $293\text{K}$ . The black body is temperature stabilised to achieve an absolute radiometric accuracy below  $1\%$ , as discussed in section 3.3. The baseline concept uses a pyramid-field black body, similar to the one described in (Olschewski *et al.* 2013).

## 4. Mission Design

In order to fulfil the science requirements stated in chapter 2, the system should achieve a revisit time of at least 4 hr, and ensure a lifetime of 5 years.

### 4.1. Launch Strategy and Orbit Injection

To achieve the science goals, a constellation of three Sun-Synchronous WAVE-E satellites was designed. Each satellite has an orbit altitude of  $817 \text{ km}$  and a corresponding inclination is  $98.7 \text{ deg}$ , with a RAAN difference of  $60 \text{ degrees}$  between the orbital planes (namely  $63.8, 123.8, \text{ and } 183.8 \text{ degrees}$  respectively). This yields a revisit time of  $4 \text{ hr}$  and an orbital period of  $101.54 \text{ minutes}$ .

The chosen launch strategy first places one satellite in orbit and later the other two satellites. This is not only appealing from the  $\Delta V$  budget perspective, but also for risk management purposes. Thus, the first satellite is launched individually with a Vega rocket and injected directly into the desired orbit. Following the Operational Readiness Review (ORR) of the first satellite, satellite two and three enter phase D to be later launched together in a Vega rocket to an orbit perpendicular to the first satellite's orbit. In order to reach the desired RAAN values, a manoeuvre will then be performed to change the inclination of satellites two and three by  $1.5 \text{ degrees}$ , such that the orbits will no longer be exactly sun-synchronous and the Earth's J2 effect

will be used to naturally drift their respective RAAN angles. After 6 months, the RAAN will have drifted as required and the inclination can be changed back so the satellites can remain in the desired SSO orbit.

#### 4.2. $\Delta V$ budget and Propulsion Subsystem

The  $\Delta V$  budget can be seen below in Table 5. It should be noted that maximum Vega injection error is 15 km altitude and 0.15 degrees inclination. Moreover, due to the different launch strategies, the WAVE-E2 and WAVE-E3 must provide 204.62m/s greater  $\Delta V$  than WAVE-E1 (including a 5% margin). This results in the tank mass and volume shown in Table 6. Despite the difference in propellant volumes, the propulsion subsystem was designed to fit all three satellites. Thus, it was decided to incorporate the monopropellant tank Model OST 31/0 (which can fit 104 to 177 litres), together with a pressurant tank, pressurant gas, 12 thrusters (4 for redundancy), valves (12 main valves as well as 8 safety valves), and piping (7.5% of the tank mass was assumed for calculations). For each of these, commercially available systems were selected, which added up to a total system mass of 32 kg, with a peak power consumption of 10 W (1.25 W per thruster, with a maximum of 8 active thrusters). It should also be noted that in the  $\Delta V$  budget an accommodation was made for *Collision Avoidance* of two collisions per year with a 2m/s of  $\Delta V$  per avoidance. This is justified by the fact that the models for space debris from ESA show that the region from 800 to over 1000km is going to be affected by those in the next few years.

**Table 5.**  $\Delta V$  Budget

	$\Delta V$ w/o margin [m/s]	margin	$\Delta V$ [m/s]
Launcher Error	27.3	5%	28.6
Initial Detumbling	10.0	100%	20.0
Orbital transfers	0 (194.9)	5%	0 (204.6)
Drag maintenance	10.9	5%	11.4
Attitude control	44.0	100%	88.0
M. wheel unloading	44.0	100%	88.0
Deorbit EoL	90.0	5%	94.5
Collision avoidance	44.0	5%	46.2
		Total [m/s]	376.8 (581.4)

**Table 6.**  $\Delta V$ , propellant mass and propellant volumes per satellite

	WAVE-E1	WAVE-E2&3
Mprop [kg]	67.5	109.1
Volume [L]	89.1	144.1

#### 4.3. ADCS

The driving system requirements that impact the attitude determination and control system of the satellite are a pointing stability of 3 arcseconds over 0.3 seconds at  $1\sigma$  confidence level, as well as a pointing knowledge of 20 arcseconds per axis. The ADCS system needs to maintain the attitude of the satellite in the presence of time-varying external disturbance torques such as solar radiation pressure and aerodynamic drag, which will be the main torques in the presence of a large deployable solar array.

The main sensors used for determination of the attitude and the position are the inertial measurement unit, three star trackers and a 2-band GPS receiver with redundancy. According to instrument specifications, the angular rates will be measured with a resolution of 0.01 arcseconds, the pointing angle with a resolution of 1 arcseconds per axis and the position within 12 metres.

The attitude is controlled by a set of 4 momentum wheel assemblies, providing a torque of 40 mNm per axis and momentum storage of 4.8 Nms. The fuel budget includes propellant used for momentum dumping using the 12 thrusters that will be used both for the attitude control as well as orbital control.

Depending on the mission stage and the condition of the satellite, it will operate in different modes. In an initial attitude acquisition or failure mode, the wheels are used together with the thrusters to reject high angular rates and attitude errors. In the nominal mode, the wheels are the main source of attitude torque with the thrusters used for momentum dumping. In the orbital manoeuvre mode, the wheels are used to reorient the spacecraft while the thrusters are used for translation.

#### 4.4. Electrical Power System

The satellite is powered by a NeXt Triple Junction solar cell array and by Li-Ion batteries for eclipse periods. The 3.2m<sup>2</sup> array is dimensioned in order to generate enough power for all the subsystems and the payload to function nominally at end of life. Should the mission be extended, it would be with reduced functionality. Any excess power generated by the solar array typically at beginning of life will need to be shunted. The array outputs around 950W at BOL and 650W at EOL.

The secondary power system relies on two 28Ah Li-Ion batteries. The batteries are dimensioned according to mission requirements and will only be discharged to 30% to ensure a lifetime of around 50 000 cycles.

Both the solar cells and the batteries provided by Spectrolab and by Saft respectively have been flown in LEO and GEO missions and have a high technology readiness level.

The mass and power requirements of the EPS system are summarised in Table 7.

#### 4.5. Communication

For the WAVE-E instrument data rate, a value of 1.2 kbps is expected. Together with usual Housekeeping data, this gives an estimated 563 Megabytes per orbit and 8.0 Gigabytes per day. Generated telemetry data can be stored on mass memory storage for further downlinking.

A S-band transceiver was chosen for the telemetry and telecommanding radio due to its widely availability and high TRL. Due to the low data rate requirements of the scientific payload, TM downlink bit rate 10 Mbits/s and uplink bit rate of 1 Mbit/s to ensure robustness of the link. The link utilizes half rate concatenated error correction coding with outer convolutional and inner Reed-Solomon coding to achieve bit error rate (BER) less than  $10^{-7}$ . Also higher order PSK (Quadrature Phase Shift Keying, QPSK) modulation was chosen to compensate the increased bitrate.

The needed transmitter RF power is 10 watts with a low-gain nadir pointing helix antenna which side lobes points to horizon allowing a reliable link without accurate pointing. A simplified link budget for up- and downlink is represented in Table 7.

Further analysis is needed to evaluate possible need for a higher speed downlink to X-band depending on final scientific telemetry data rate and possible link time limitations.

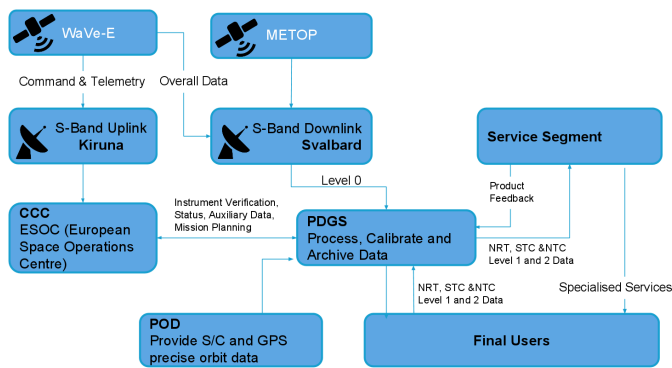
**Table 7.** Simplified Link Budget

	Uplink	Downlink
Frequency	2.0 GHz	2.2 GHz
Data rate	1 Mbit/s	10 Mbit/s
Tx RF Power	~ 30 W	10 W
Tx Total losses	-0.6 dB	-1.9 dB
Total path losses	-169.3 dB	-170.2 dB
EIRP	98 dBm	14.5 dBm
Rx G/T	7.4 dB/K	23 dB/K
$E_b/N_0$	46.4 dB	18.4 dB
Required $E_b/N_0$	6 dB	6 dB
<b>Margin</b>	<b>40.4 dB</b>	<b>12.4 dB</b>

#### 4.6. Ground Segment and Operations

WAVE-E mission is planned to be operate via ESA's Svalbard and Kiruna ground stations, which are located in high latitudes and have a good visibility for polar orbits. Total link time per day is estimated to be roughly 160 minutes which is sufficient for full operations of WaVe-E.

Mission operation is planned to happen in ESA's ESOG operation centre in Darmstadt, Germany. The ground operations data processing is done to produce level 1-4 data products for the end-users. Ground segment operations and data flow is represented in Table 9.


**Fig. 9.** Ground Segment and Operations

#### 4.7. Thermal Control

The thermal balance has not been determined in detail, but since the satellite is on a sun-synchronous orbit it will periodically enter both lit and eclipsed areas. The subsystems have both lower and upper temperature ranges to ensure functionality, and so the temperature will need active control to remain within these boundaries. Multi-layer insulation (MLI) is used to cover the satellite in order to reflect any incoming or out-going radiation. A passive radiator panel will be placed on a side of the satellite that will always face away from both the Sun and the Earth to radiate excess heat generated on-board. The only active components, apart from the coolers which are accounted for in the payload section, are heaters used to keep critical components heated during eclipse.

#### 4.8. Onboard Command and Data Handling

The Onboard Command and Data Handling (OCDH) subsystem has two core functions: to gather and format satellite housekeeping data for down-link and to receive and distribute commands from the up-link. The hardware consists of a Mass memory unit

provided by Surrey with 256 GB of non-volatile storage memory to store the science and house-keeping data before down-linking it during the 11 minute pass over the Svalbard ground station. The OBC Panther processor board manufactured by RUAG will be used to control the satellite. The SSTL-300 satellite platform seems highly compatible with the payload and core subsystems, and is a design option that should be considered. This will have additional benefits in terms of cost reduction, being off-the-shelf ready. All of the OCDH hardware is radiation-hardened and well suited for the intended environment, and a redundant set shall be installed for safety.

#### 4.9. Mass and Power budget

Given the characteristics of all subsystems as described above, the final mass and power budget are listed in Table 8. The largest part of the mass and power budget belong to the payload. In this early stage of the design phase and so the margins are quite large, especially for the payload. Most subsystems are using off-the-shelf hardware and can be determined with higher confidence.

It must be noted that the propellant tank is large enough to hold the extra fuel required in satellites 2 and 3, meaning the dry mass is identical between the three satellites. Mass differences between the satellites is represented in Table 6.

**Table 8.** Mass and Power Budget

Subsystem [margin]	Mass [kg]	Power [W]
Payload [30%]	103.0	110.2
Structure [25%]	50.4	3.3
Harnessing [25%]	17.6	-
Thermal [25%]	8.6	35.2
EPS [10%]	31.8	28.2
Comms [10%]	9.9	37.6
OBDR [10%]	33.0	31.2
ADCS [10%]	19.0	31.3
Propulsion [10%]	35.8	12.0
<b>Dry Mass / Power (20% system margin)</b>	<b>309.3</b>	<b>288.88</b>
Propellant (WAVE-E1)	68	-
Propellant (WAVE-E2&3)	110	-
<b>Total Mass &amp; Power (WAVE-E1)</b>	<b>438</b>	<b>346.7</b>
<b>Total Mass &amp; Power (WAVE-E2/3)</b>	<b>480</b>	<b>346.7</b>

#### 4.10. Programmatics

10 depicts the programmatics of the baseline mission. WAVE-E1 will be launched before 2025 and has a lifetime of 5 years. Depending on the status of the mission in 2017 and provided that the data provided is still valuable and funds are available to continue operations, the mission could be extended as there are enough consumables for 11 years. After commission of the first satellite, production of WAVE-E2 and WAVE-E3 could begin, with Phase D being shorter than for the first satellite. Calibration activities can be performed simultaneously using the Air WAVE-E Cal/Val campaign. Moreover, the measurements can be fed into the Global Space-based Inter-Calibration System (GSICS). Furthermore, early adopters experiments can also begin at the same time to enhance the assimilation of water vapour at ECMWF.

Thus, WAVE-E2 and WAVE-E3 will be launched 2 years afterwards and will require another 6 months of orbital manoeuvring. Although this will reduce coverage while WAVE-E1 is

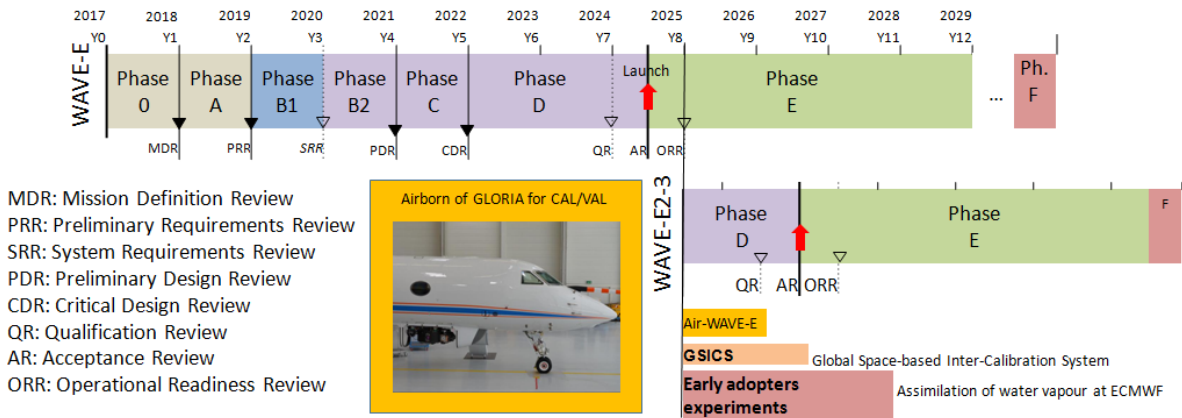


Fig. 10. Programmatics and timeline of the mission

Table 9. Risk analysis of critical components

Risk	Severity	Impact	Mitigation
Orbital injection failure	1	4	Thruster redundancy, wide fuel margins
Momentum wheel failure	2	4	Redundancy
Thruster malfunction	3	4	Redundancy
Solar flare damages computer	2	5	Redundancy & space qualified parts
Payload malfunction	1	4	Comprehensive qualification testing
Star trackers failure	2	4	Redundancy
Software failure	3	4	Formal software qualification testing

Table 10. Preliminary ROM Estimate

Item	Cost [M€]
Project Team	50
Industrial Cost with Instrument	300
Mission & Science Oper.	75
Contingency	75
Total ROM	500
Launcher (2x Vega)	80
<b>Grand Total ROM (with launch)</b>	<b>580</b>

alone, it will ensure that scientific data is provided longer than the mission requirement without necessarily extending its life-time.

To comply with ESA regulations, an additional 90 m/s of  $\Delta V$  is allocated in each satellite to be actively de-orbited at EoL. This maneuver will lower the perigee from 817 km to 480 km, where atmospheric drag will naturally lower the satellite’s altitude until re-entry in 21 years.

#### 4.11. De-scoping

The main objective of this mission design is to provide a three-satellite constellation. A de-scoping option would be to reduce the number of satellites to a single one in orbit. This leads to a decrease of temporal resolution.

#### 4.12. Cost and Risk Analysis

##### 4.12.1. Risk Analysis

An overview of the mission risk analysis can be seen in Table 9, as well as the corresponding mitigation factor. Nonetheless avoidance of single point failure should be implemented as far as it is practical.

##### 4.12.2. Preliminary Cost Analysis

As a Rough Order of Magnitude (ROM) cost estimate, the estimate that 1 kg of payload corresponds to 1M Euro cost was used, and the cost built up as shown in Table 10.

For the additional 2 satellites, it was assumed that their combined cost would be 80M Euros, due to the fact that they would no longer be incurring development costs, just the production. Another point to note is that official Vega launch costs have not yet been released, so 40M Euros per launch is an estimate only. It should also be considered that there are many potential areas for cost reduction which could be explored; using off-the-shelf components, for instance, will be cheaper in terms of having little development cost.

## 5. Conclusions

WAVE-E (Water Vapour European – Explorer) is a new mission concept optimized for the observation of water vapour in the UTLS region, bringing original data that will fill in the gap in water vapour observation in the atmosphere (Kidston *et al.* 2015). The data from WAVE-E will improve our understanding of the interactions between the troposphere and stratosphere that are at the origin of many extreme weather and climate events linked to the water cycle. WAVE-E will provide water vapour profiles in the UTLS with an uncertainty of 10%, a vertical resolution of 1 km and at a 4h temporal frequency. The proposed mission consists of three small satellites (~ 500kg) to be launched attached to a spacecraft which will fit inside a Vega launcher and place it at a sun-synchronous orbit. The main products from WAVE-E will be assimilated into weather prediction and climatological models to help advance the science in the domain and bring concrete and quantifiable societal impact by improving the prediction of extreme weather events. The mission is configured to have the capability to follow the METOP-NG satellites to produce combined synergistic products, though this is not a requirement for accomplishing the primary objectives of the mission.

## References

- J. Kidston, A. A. Scaife, S. C. Hardiman, D. M. Mitchell, N. Butchart, M. P. Baldwin, and L. J. Gray, *Stratospheric influence on tropospheric jet streams, storm tracks and surface weather*, *Nature Geoscience* **8**, 433 (2015).
- A. G. Marshall and A. A. Scaife, *Improved predictability of stratospheric sudden warming events in an atmospheric general circulation model with enhanced stratospheric resolution*, *J. Geophys. Res.* **115** (2010).
- R. Müller, A. Kunz, D. F. Hurst, C. Rolf, M. Krämer, and M. Riese, *The need for accurate long-term measurements of water vapor in the upper troposphere and lower stratosphere with global coverage*, *Earth's Future* **4**, 25 (2016).
- J. H. Jiang, H. Su, C. Zhai, L. Wu, K. Minschwaner, A. M. Molod, and A. M. Tompkins, *An assessment of upper troposphere and lower stratosphere water vapor in MERRA, MERRA2, and ECMWF reanalyses using Aura MLS observations*, *J. Geophys. Res.-Atmos.* **120**, 11,468 (2015).
- K. E. Trenberth, L. Smith, T. Qian, A. Dai, and J. Fasullo, *Estimates of the Global Water Budget and Its Annual Cycle Using Observational and Model Data*, *J. Hydrometeor.* **8**, 758 (2007).
- I. M. Held and B. J. Soden, *WATER VAPOR FEEDBACK AND GLOBAL WARMING I*, *Annu. Rev. Energ. Env.* **25**, 441 (2000).
- G. A. Schmidt, R. A. Ruedy, R. L. Miller, and A. A. Lacis, *Attribution of the present-day total greenhouse effect*, *J. Geophys. Res.* **115** (2010).
- E. P. Gerber, C. Orbe, and L. M. Polvani, *Stratospheric influence on the tropospheric circulation revealed by idealized ensemble forecasts*, *Geophys. Res. Lett.* **36** (2009).
- ESA-GWEX, *Easth Observation and Water Cycle Priorities*, (2015).
- M. Hegglin, D. Plummer, T. Shepherd, J. Scinocca, J. Anderson, L. Froidevaux, B. Funke, D. Hurst, A. Rozanov, J. Urban, et al., *Vertical structure of stratospheric water vapour trends derived from merged satellite data*, *Nature Geoscience* **7**, 768 (2014).
- O. P. Tripathi, M. Baldwin, A. Charlton-Perez, M. Charron, J. C. H. Cheung, S. D. Eckermann, E. Gerber, D. R. Jackson, Y. Kuroda, A. Lang, J. McLay, R. Mizuta, C. Reynolds, G. Roff, M. Sigmond, S.-W. Son, and T. Stockdale, *Examining the predictability of the stratospheric sudden warming of January 2013 using multiple NWP systems*, *Mon. Wea. Rev.* **144**, 1935 (2016).
- P. Hassanzadeh, Z. Kuang, and B. F. Farrell, *Responses of midlatitude blocks and wave amplitude to changes in the meridional temperature gradient in an idealized dry GCM*, *Geophys. Res. Lett.* **41**, 5223 (2014).
- D. Hartmann, A. Klein Tank, M. Rusticucci, L. Alexander, S. Brönnimann, Y. Charabi, F. Dentener, E. Dlugokencky, D. Easterling, A. Kaplan, B. Soden, P. Thorne, M. Wild, and P. Zhai, *Climate Change 2013: The Physical Science Basis. Contribution of Working Group I to the Fifth Assessment Report of the Intergovernmental Panel on Climate Change*, in *Observations: Atmosphere and Surface*, edited by T. Stocker, D. Qin, G.-K. Plattner, M. Tignor, S. Allen, J. Boschung, A. Nauels, Y. Xia, V. Bex, and P. Midgley (Cambridge University Press, 2013).
- B. Bolin and H. Rodhe, *A note on the concepts of age distribution and transit time in natural reservoirs*, *Tellus* **25**, 58 (1973).
- E. Andersson, *User guide to ECMWF forecast products*, 1st ed. (ECMWF, Livelink 4320059, 2015).
- EUMETSAT, *The Metop satellites carry a set of state-of-the-art sounding and imaging instruments that offer improved remote sensing capabilities to both meteorologists and climatologists*, (2016).
- C. Clerbaux, A. Boynard, L. Clarisse, M. George, J. Hadji-Lazaro, H. Herbin, D. Hurtmans, M. Pommier, A. Razavi, S. Turquety, C. Wespes, and P.-F. Coheur, *Monitoring of atmospheric composition using the thermal infrared IASI/MetOp sounder*, *Atmospheric Chemistry and Physics* **9**, 6041 (2009).
- C. Crevoisier, C. Clerbaux, V. Guidard, T. Phulpin, R. Armante, B. Barret, C. Camy-Peyret, J.-P. Chaboureaud, P.-F. Coheur, L. Crépeau, G. Dufour, L. Labonnote, L. Lavanant, J. Hadji-Lazaro, H. Herbin, N. Jacquinet-Husson, S. Payan, E. Péquignot, C. Pierangelo, P. Sellitto, and C. Stubenrauch, *Towards IASI-new generation (IASI-NG): impact of improved spectral resolution and radiometric noise on the retrieval of thermodynamic, chemistry and climate variables*, *Atmos. Meas. Tech.* **7**, 4367 (2014).
- H. Herbin, D. Hurtmans, C. Clerbaux, L. Clarisse, and P.-F. Coheur, *H<sub>2</sub>O and HDO measurements with IASI/MetOp*, *Atmospheric Chemistry and Physics* **9**, 9433 (2009).
- W. OSCAR, *Instrument details: IASI*, (2016).
- ESA, *Report for Mission Selection: PREMIER, ESA SP-1324/3 (3 volume series)*, European Space Agency, Noordwijk, The Netherlands. (2012).
- T. von Clarmann, M. Höpfner, S. Kellmann, A. Linden, S. Chauhan, B. Funke, U. Grabowski, N. Glatthor, M. Kiefer, T. Schieferdecker, G. P. Stiller, and S. Versick, *Retrieval of temperature, h<sub>2</sub>o, o<sub>3</sub>, hno<sub>3</sub>, ch<sub>4</sub>, n<sub>2</sub>o, clono<sub>2</sub> and clo from MIPAS reduced resolution nominal mode limb emission measurements*, *Atmos. Meas. Tech.* **2**, 159 (2009).
- NOAA, *US standard atmosphere* (U.S. Government Printing Office, 1976).
- L. Rothman, I. Gordon, Y. Babikov, A. Barbe, D. C. Benner, P. Bernath, M. Birk, L. Bizzocchi, V. Boudon, L. Brown, A. Campargue, K. Chance, E. Cohen, L. Coudert, V. Devi, B. Drouin, A. Fayt, J.-M. Flaud, R. Gamache, J. Harrison, J.-M. Hartmann, C. Hill, J. Hodges, D. Jacquemart, A. Jolly, J. Lamouroux, R. L. Roy, G. Li, D. Long, O. Lyulin, C. Mackie, S. Massie, S. Mikhailenko, H. Müller, O. Naumenko, A. Nikitin, J. Orphal, V. Perevalov, A. Perrin, E. Polovtseva, C. Richard, M. Smith, E. Starikova, K. Sung, S. Tashkun, J. Tennyson, G. Toon, V. Tyuterev, and G. Wagner, *The HITRAN2012 molecular spectroscopic database*, *J. Quant. Spectrosc. Ra.* **130**, 4 (2013).
- E. Endemann, *MIPAS Instrument Concept and Performance*, (1999).
- T. L. Killeen, W. R. Skinner, R. M. Johnson, C. J. Edmonson, Q. Wu, R. J. Niciejewski, H. J. Grassl, D. A. Gell, P. E. Hansen, J. D. Harvey, and J. F. Kalkalidis, *TIMED Doppler interferometer (TIDI)*, (1999) pp. 289–301.
- H. Fischer, M. Birk, C. Blom, B. Carli, M. Carlotti, T. von Clarmann, L. Delbouille, A. Dudhia, D. Ehhalt, M. Endemann, J. M. Flaud, R. Gessner, A. Kleinert, R. Koopman, J. Langen, M. López Puertas, P. Mosner, H. Nett, H. Oelhaf, G. Perron, J. Remedios, M. Ridolfi, G. Stiller, and R. Zander, *MIPAS: an instrument for atmospheric and climate research*, *Atmospheric Chemistry and Physics* **8**, 2151 (2008).
- G. G. Shepherd, G. Thuillier, W. A. Gault, B. H. Solheim, C. Hersom, J. M. Alunni, J.-F. Brun, S. Brune, P. Charlot, L. L. Cogger, D.-L. Desaulniers, W. F. J. Evans, R. L. Gattinger, F. Girod, D. Harvie, R. H. Hum, D. J. W. Kendall, E. J. Llewellyn, R. P. Lowe, J. Ohrt, F. Pasternak, O. Peillet, I. Powell, Y. Rochon, W. E. Ward, R. H. Wiens, and J. Wimperis, *WINDII, the wind imaging interferometer on the Upper Atmosphere Research Satellite*, *J. Geophys. Res.* **98**, 10725 (1993).
- P. Connes, *Spectromètre interférentiel à sélection par l'amplitude de modulation*, *J. Phys. Radium.* **19**, 215 (1958).
- J. Harlander, R. J. Reynolds, and F. L. Roesler, *Spatial heterodyne spectroscopy for the exploration of diffuse interstellar emission lines at far-ultraviolet wavelengths*, *Astrophys. J.* **396**, 730 (1992).
- J. M. Harlander, F. L. Roesler, J. G. Cardon, C. R. Englert, and R. R. Conway, *Shimmer: A Spatial Heterodyne Spectrometer for Remote Sensing of Earth's Middle Atmosphere*, *Appl. Optics.* **41**, 1343 (2002).
- R. A. Doe and S. Watchorn, *Climate-monitoring CubeSat mission (CM2): a project for global mesopause temperature sensing*, in *Earth Observing Systems XVI*, edited by J. J. Butler, X. Xiong, and X. Gu (SPIE-Intl Soc Optical Eng, 2011).
- C. R. Englert, J. M. Harlander, C. Brown, J. Makela, K. Marr, and T. Immel, *MIGHTI: The Spatial Heterodyne Instrument for Thermospheric Wind Measurements on Board the ICON Mission, in Fourier Transform Spectroscopy and Hyperspectral Imaging and Sounding of the Environment* (The Optical Society, 2015).
- C. R. Englert, J. M. Harlander, J. C. Owrutsky, and J. T. Bays, *SHIM-Free Breadboard Instrument Design, Integration, and First Measurements*, (2005).
- G. G. Shepherd, *Spectral imaging of the atmosphere* (Academic Press, San Diego, Calif, 2002).
- R. D. Nibir K. Dhar, Ashok K. Sood, *Advances in Infrared Detector Array Technology* (INTECH Open Access Publisher, 2013).
- F. Olschewski, A. Ebersoldt, F. Friedl-Vallon, B. Gutschwager, J. Hollandt, A. Kleinert, C. Monte, C. Piesch, P. Preusse, C. Rolf, P. Steffens, and R. Koppmann, *The in-flight blackbody calibration system for the GLORIA interferometer on board an airborne research platform*, *Atmos. Meas. Tech.* **6**, 3067 (2013).